Processes regulating formation of low-salinity high-biomass lenses near the edge of the Ross Ice Shelf

Yizhen Li[1], Dennis J. McGillicuddy Jr. [1], Michael S. Dinniman[2], and John M. Klinck[2]
[1]Department of Applied Ocean Physics and Engineering, Woods Hole Oceanographic Institution, Woods Hole, MA 02543
[2]Center for Coastal Physical Oceanography, Old Dominion University, Norfolk, Virginia 23529, USA

Correspondence: Yizhen Li, Phone: 508-289-2238, Email: yzli@whoi.edu

Abstract

In situ observations in austral summer of early 2012 in the Ross Sea suggest the presence of low-salinity, high-biomass lenses within cold eddies along the edge of the Ross Ice Shelf (RIS). Idealized model simulations are utilized to examine the processes responsible for ice shelf eddy formation. 3-D model simulations produce similar cold and fresh eddies, although the simulated vertical lenses are quantitatively thinner than observed. Model sensitivity tests show that both basal melting underneath the ice shelf and irregularity of the ice shelf edge facilitate generation of cold and fresh eddies. 2-D model simulations further suggest that both basal melting and downwelling-favorable winds play crucial roles in forming a thick layer of low-salinity water observed along the edge of the RIS. These properties may have been entrained into the observed eddies, whereas that entrainment process was not captured in the specific eddy formation events studied in our 3-D model—which may explain the discrepancy between the simulated and observed eddies, at least in part. Additional sensitivity experiments imply that uncertainties associated with background stratification and wind stress may also explain why the model underestimates the thickness of the low-salinity lens in the eddy interiors. Our study highlights the importance of incorporating accurate wind forcing, basal melting and ice shelf irregularity for simulating ocean dynamics near the RIS edge.

Key words: eddies, instability, basal melting, mixed layer processes, ice shelf geometry

1. Introduction

Ice shelves are floating extensions of grounded glaciers. The largest ice shelf (~4.7× 10^5 km^2) in Antarctica is the Ross Ice Shelf (RIS), located in the southern Ross Sea (Fig. 1). The RIS region plays host to a number of important physical and biological processes. Air-sea interaction and ice dynamics at the edge of the RIS influence High Salinity Shelf Water (HSSW) formation (MacAyeal, 1984; Orsi and Wiederwohl, 2009), which is a dense water mass that is critical in Antarctic Bottom Water formation (Jacobs et al., 1996; Orsi et al., 2002; Whitworth and Orsi, 2006; Gordon et al., 2009). The frontal region also bridges heat and mass exchanges with the open ocean (Shepherd et al., 2010, 2012; Rignot et al., 2013; Depoorter et al., 2013). The Ross Sea is the most productive area in the Southern Ocean (Comiso et al., 1993; Arrigo et al., 1998), and the RIS delimits the southern boundary of the region of high productivity. Although recent evidence suggests that the iron supply from glacial ice melt constitutes only a small fraction of the iron supply to the entire Ross Sea (McGillicuddy et al., 2015), basal melting is a primary pathway for iron supply in other Antarctic polynyas (Arrigo et al., 2015; Gerringa et al., 2012).

Processes at different depth levels make the cavity underneath the RIS a unique ocean environment. In the surface ocean layer, basal melting is facilitated by occasional warm water intrusions (Jenkins and Doake, 1991, Horgan et al., 2011; Arzeno et al., 2014). At mid depth, melting is caused by intrusion of modified circumpolar deep water (Jacobs et al., 2011, Dinniman et al., 2007, 2012; Klinck and Dinniman, 2010; Pritchard et al., 2012). In the deepest layer, dense HSSW (a product of brine rejection over the continental shelf from ice formation during the winter months), which is at the surface freezing point, can penetrate into the cavity, causing melting near the grounding line due to the depression of the freezing point of seawater with increasing pressure. As the buoyant meltwaters rise along the ice shelf base, they can re-freeze at mid-depth due to the increase in freezing point with decreasing pressure, producing super-cooled Ice Shelf Water (ISW). All these processes interact with each other at various spatial and temporal scales, making for a complex regime of thermohaline circulation (MacAyeal, 1984; 1985).

Of particular interest from a coupled physical-biological perspective is the penetration of glacial meltwater into the surface waters in the interior of the Ross Sea, as this constitutes a source of iron to upper ocean phytoplankton populations. In austral summer of 2012, we observed two anticyclonic eddies emanating from the edge of the RIS northward into the Ross Sea. These low-salinity lenses had deep mixed layers (ca. 80 m) and very high biomass of the colonial prymnesiophyte *Phaeocystis antarctica* (Smith et al., in preparation). Our goal is to identify the processes that lead to generation of these eddy features, taking an initial step toward understanding their importance to the physics and biology of the region.

The primary surface circulation feature along the front of the RIS in this area is a relatively strong, narrow and fresh, westward flowing coastal current (Jacobs et al., 1970; Keys et al., 1990). A similar westward current is found along the front of the Ronne-Filchner Ice Shelf (Makinson et al., 2006) where mooring observations at depth also suggest the possibility of eddy derived variability (Nicholls et al., 2003). Knowledge of ocean variability in the near-surface ocean layer near the RIS remains rather limited due the scarcity of data, with relatively few direct observations available (Jacobs et al., 1985; Smethie and Jacobs, 2005). Arzeno et al. (2014) postulated eddies as being responsible for variability in currents underneath the RIS that was uncorrelated with the wind. Although the process of eddy generation has been examined in many oceanic regimes, relatively few studies have focused on instabilities associated with ice-ocean interactions (Clarke et al., 1978; Chu, 1987; Dumont et al., 2010; Häkkinen, 1986; Niebauer, 1982). In general, glacial meltwater can create horizontal density gradients that force a baroclinic jet (Niebauer, 1982). Häkkinen (1986) found that when across- and along-ice edge spatial scales are similar enough, such baroclinic jets can generate eddy structures along the ice edge, especially when the wind forcing is time-varying between upwelling and downwelling conditions. In a modeling study in Baffin Bay near Greenland, cyclonic eddies were generated at the edge of landfast ice in response to strong wind forcing (Dumont et al., 2010). All of these studies pointed to the importance of baroclinic jets and wind forcing in forming eddies near the ice edge.

Earlier efforts utilized idealized two-layer ocean models to study how ice-ocean interactions can excite unstable wave forms. Using a semi-analytical quasi-geostrophic model, Clark et al. (1978) showed that fluctuations in the flow along fast ice can be described as wind-forced trapped long-waves propagating along the ice edge. Chu (1987) used a similar framework, identifying an air-sea interaction feedback mechanism that excites an unstable mode in the presence of curvature in the ice edge. Their work highlighted the importance of considering multiple factors such as ice shelf edge irregularity and background stratification (initial conditions) in studying the instability processes. However, because their models did not consider basal melting, they were not able to capture the structure of low salinity features near the ice edge.

Our approach is to use high-resolution models with varying levels of complexity to understand the mesoscale phenomena we observed at the edge of the RIS. In section 2 we present the observations, consisting of both satellite imagery and *in situ* measurements. We describe the model configuration in section 3, followed by sections 4 and 5 showing its implementation in three- and two-dimensional configurations respectively. The former is used to investigate the process responsible for eddy generation, whereas the latter provides insight into the mechanisms responsible for the thickness of the low-salinity surface layer. Section 6 offers further analysis and discussion of the dynamics via sensitivity analyses. A summary and conclusions are presented in section 7.

2. Observations

2.1 Satellite imagery

A sequence of satellite images in January 2012 captured the signature and evolution of several eddies near the RIS. On January 22, there were a number of cold eddies along the edge of the ice shelf (Fig. 2a), including some that were already separated from the RIS (e.g., near 177.5°E), and some that remained connected to the ice shelf edge (e.g., Eddy 1 and Eddy 2). Eddy 1 (radius ~12 km) was flanked by warm anomalies to the east and northwest. Eddy 2 was slightly smaller (radius ~8 km), separated from Eddy 1 by a warm filament protruding south to the edge of the RIS. Satellite ocean color imagery indicated a ca. 20 km wide strip of low chlorophyll *a* (Chl-a) concentrations extending along the edge of the RIS, with much higher concentrations to the north (Fig. 2b). The signatures of Eddies 1 and 2 in ocean color are barely discernible in the January 22 image as northward perturbations to the frontal boundary separating high and low Chl-a.

Three days later, the two eddies had moved away from the RIS and evolved in the process (Fig. 3). Eddy 1 moved north, whereas Eddy 2 moved northwest, narrowing the gap in between them. Both eddies propagated westward, as is commonly the case (Cushman-Roisin et al., 1990). Compared to three days prior, Eddy 1 took on a more circular shape. By January 25, Eddy 1 had almost completely separated from the RIS, connected to the shelf edge by only a narrow cold filament running southwest from the southern flank of the eddy (Fig. 3a). The warm anomaly previously to the east of Eddy 1 on January 22 appeared to have been swept southwestward by January 25. However, this movement is opposite in direction to that caused by the eddy's rotation, so if this interpretation is correct then translation of the warm anomaly must have been caused by flow external to the eddy. Whereas Eddy 1 had almost entirely separated from the RIS on January 25, Eddy 2 was still in the process of separation from the ice shelf, with a cold filament linking its southern flank to the cold-water band adjacent to the RIS. As the two eddy features moved away from the RIS into the Ross Sea interior, they became more clearly evident in ocean color imagery as local minima in Chl-a (Fig. 3b).

2.2 High-resolution survey of the RIS eddies

Voyage NBP-1201of RVIB *Nathaniel B. Palmer* took place from December 24, 2011 to Feb 5, 2012. A multi-scale survey of the Ross Sea was carried out, and herein we focus on a subset of the observations collected in the vicinity of the RIS. High-resolution cross-sections of Eddies 1 and 2 were obtained with the Video Plankton Recorder (VPR; Davis et al., 1992), providing conductivity, temperature and depth (CTD) observations, along with fluorescence measurements and plankton imagery. Underway Acoustic Doppler Current Profiler (ADCP) current velocity observations were collected along the ship track with an RD Instruments NB150. Hydrographic profiles were obtained with a SeaBird Electronics 911 CTD and standard rosette system.

A VPR survey of Eddies 1 and 2 was conducted on January 26 (magenta line, Fig. 3). The ship track started from the west and cut through Eddy 1. It then passed across the frontal area between the two eddies, penetrated into the interior of Eddy 2, and subsequently turned southeastward. ADCP currents (Fig. 3) showed that both eddies were anticyclonic (counter-clockwise). The VPR data revealed that the cores of both eddies contained low-salinity lenses extending from the surface to 80 m (Fig. 4b). The surface layer temperature was 0.6 ℃ lower than outside of the eddies (Fig 4a). The mixed layers within the eddies were deeper than outside, where the surface layer of relatively warm and salty water was only about 45 m deep (Fig. 4a, b). The cold and fresh lenses in the eddy interiors contained high fluorescence (Fig. 4c), consistent with high abundance of *P. antarctica* colonies identified in the VPR imagery (Smith et al., in prep). Highest fluorescence along the ship track occurred at the frontal boundary on the western flank of Eddy 2, although the mechanism responsible for that submesoscale enhancement remains unknown.

It is interesting to note that the lenses of high fluorescence revealed by the VPR data (Fig. 4c, d) were manifested as local minima in Chl-a in the satellite imagery (Fig. 3). Caution needs to be taken in comparing *in situ* fluorescence and satellite data for several reasons. First, the algorithm for retrieving MODIS Chl-a is based on water leaving irradiance (Clark, 1997), and the Chl-a concentration reflects a weighted average over the upper 1-2 optical depths. Second, remotely sensed Chl-a can also be contaminated by other dissolved and particulate materials (Carder et al., 2004). Finally, *in vivo* fluorescence can be reduced by the ‘quenching effect’ (e.g., Falkowski et al., 1995) when photosynthetic reaction centers are saturated with ambient light, such as typically occurs in the upper euphotic zone during daylight hours.

Despite these caveats, it is still of interest to make direct comparisons between the VPR observations of fluorescence and the satellite retrievals of Chl-a. The optical depth can be estimated based on an inverse relationship with the attenuation coefficient of downward irradiance (K_d) for blue light (http://oceancolor.gsfc.nasa.gov/cms/atbd/kd_490). Based on satellite data from January 2012, K_d was within the range of 0.2-0.4 m^{-1} near the RIS edge (not shown), indicating an optical depth of ~5 m. Comparison of the VPR fluorescence averaged over upper two optical depths (10 m) and the satellite-based Chl-a concentration extracted along the VPR transect reveals similarity between two variables (Fig. 4d). Both VPR fluorescence and MODIS Chl-a were highest near the frontal region between the two eddies. Clearly, the satellite observations do not reflect the deeper structure of the fluorescence distribution (Fig. 4c) which results in a local maximum near eddy center in a depth-integrated sense (Fig. 4d).

2.3 CTD transects

In January 25-26, 2012, two CTD transects were conducted: one along the edge of the RIS, and one normal to it (Fig. 3). In general, waters along the RIS tended to be colder and fresher than those to the north (Fig. 5). However, there was considerable variability in properties along the ice shelf. At station 62, there was a cold and fresh layer extending down below 100 m, with high fluorescence throughout. This vertical structure is reminiscent of that observed in the interiors of Eddies 1 and 2, with very similar temperature and salinity characteristics.

3. Model configuration

The Regional Ocean Modeling System (ROMS, Haidvogel et al., 2008; Shchepetkin and McWilliams, 2005) is used in this study. ROMS is a free-surface, hydrostatic, primitive-equation model that employs split-explicit separation of fast barotropic and slow baroclinic modes and vertically stretched terrain-following coordinates. An ice shelf module is coupled with the ocean model (Dinniman et al., 2011; Stern et al., 2013). The *K*-profile parameterization (KPP) turbulence closure scheme (Large et al., 1994) is applied to compute both momentum and tracer vertical mixing. The KPP scheme is modified according to Dinniman et al. (2003): the surface mixed layer depth under stabilizing conditions is set to a minimum depth, equal to the directly wind forced minimum depth under stable conditions in a Kraus/Turner bulk mixed-layer model (Krauss and Turner, 1967; Niiler and Kraus, 1977). Sensitivity tests show that altering values for horizontal diffusivity within reasonable ranges have limited impact on the major conclusions herein (Appendix A). Quadratic drag is used to compute the frictional force on water in contact with the bottom and the ice shelf. The model also includes mechanical and thermodynamic interactions between the floating ice shelf and water cavity underneath (Holland and Jenkins, 1999; Dinniman et al, 2011; Stern et al., 2013). A brief description on the parameterization of the ice shelf basal melting is provided in Appendix B. Interested readers are referred to Dinniman et al. (2011) for additional details of the model.

3.1 Model grid and ice shelf

Our idealized 2-D and 3-D models of the RIS utilize the same cross-shelf geometry, configured to mimic the average bottom elevation and ice shelf draft in Bedmap2 data for the area of interest (Fig. 6), a configuration similar to that used in another idealized modeling study (Gwyther et al., 2015). Both our 2D and 3D models have 100 vertical layers, and horizontal grid resolution of 500 m in the along-ice shelf and cross- ice shelf direction (referred to as the X- and Y-directions, respectively). The horizontal resolution is approximately one order of magnitude smaller than the first baroclinic Rossby radius of deformation, thus making it suitable for simulating eddy processes at an ice shelf front (Årthun et al., 2013). The bottom is flat with a depth of 600 m. The model domains span 200 km in the cross- ice shelf direction in order to minimize impacts of the open offshore boundary on the processes of interest near the ice shelf. The 3-D model domain spans 100 km in the along- ice shelf direction. See Appendix B for additional information pertaining to accuracy of the pressure gradient calculation in this particular geometry.

3.2 Ross Ice Shelf edge roughness in the 3-D model

To implement realistic roughness in the edge of the RIS, we first digitized the edge from the Bedmap2 ice thickness (http://nora.nerc.ac.uk/501469/). Second, those roughness elements were projected onto the straight ice shelf edge in our idealized geometry.

3.3 Initial and boundary conditions

Both initial and boundary conditions (Fig.6) are spatially uniform based on the vertical temperature and salinity profiles from CTD station 58, the most offshore station for the RIS CTD survey (Fig. 5). Initial velocities and sea level elevations are set to zero. The selection of the initial condition is *ad hoc*, as the hydrographic conditions near the edge of the ice shelf were not sampled extensively. Some of the uncertainties associated with the initial condition are assessed in section 6.

A closed wall is imposed on the southern boundaries of the model domains. In the north, open boundary conditions are applied to tracers following the method of Marchesiello et al. (2001), with the external values provided by CTD station data. At the open northern boundary of both models, a 20-point sponge layer at the boundary provides enhanced viscosity and diffusivity to suppress numerical noise generated by wave reflection. The 2-D model actually includes six grid points in the along- ice shelf direction, but periodic boundary conditions yield a solution that is essentially 2-D. Periodic boundaries are also used in the 3-D model, but its 100 km extent in the along-ice shelf direction allows energetic mesoscale flows to develop. No tidal forcing is included in the model.

3.4 Surface forcing

Wind forcing is from the Antarctic meteorological station VITO on the Ross Ice Shelf (Fig. 1). The six hourly wind speed (Fig. 7) is converted to wind stress based on the formulation of Large and Pond (1981), and the wind forcing is assumed to be spatially uniform over the entire model domain. There is no surface salinity flux. A constant surface net heat flux of 35 W m^{-2} into the ocean is specified, a mean value for the month of January from the 3-D model simulations of the Ross Sea described in Dinniman et al. (2011). As we are simulating summer ice-free conditions, the sea ice module available in ROMS is turned off.

4. Numerical simulation of RIS eddies

Both satellite imagery and the *in situ* VPR observations documented the presence of the cold and fresh eddies near the RIS edge. It is therefore of interest to explore the generation mechanisms responsible for their formation. To do this, we design three experiments evaluating the relative importance of three factors: ice shelf roughness, basal melting, and surface wind stress (Table 1). Except where otherwise noted, the 3-D simulations are run for 25 days.

The baseline case includes a straight ice shelf, wind forcing, and basal melting (run SIS+WIND+BM). A cold and fresh boundary layer forms at the edge of the ice shelf due to basal melting, generating a baroclinic jet (Fig. 8 a, b), a feature similar to that described by Niebauer (1982) for a marginal sea ice edge. This is also consistent with a westward coastal jet found near the RIS front (Jacobs et al., 1970; Keys et al., 1990). Variations in surface velocity in the interior are driven by wind forcing. In this experiment, we see no evidence for generation of the types of mesoscale structures we observed (Figs. 2 and 3), even when the model was run out for an additional 60 days (not shown).

When the straight ice shelf is replaced with an irregular one (run IIS+WIND+BM), mesoscale instabilities develop in the boundary current, shedding cold and fresh eddies into the interior (Fig. 8 c, d).

To quantify the importance of wind forcing, the experiment was repeated with wind forcing turned off (run IIS+BM). Instability in the boundary current persists (Fig. 8 e, f), generating cold and fresh eddies similar those present in run IIS+WIND+BM (Fig. 8 c, d). Thus wind forcing is not necessary for eddy formation, although it does make the resulting eddies more energetic (Cf. Figs. 8c, d and 8e, f), with a domain-wide eddy kinetic energy 60% larger than the no-wind case at model day 25.

Pawlak and McCready (2002) conducted laboratory experiments to study the instabilities associated with oscillatory flow. Their results showed that oscillatory flow along an irregular coastline can change streamlines and vorticity, thus providing a mechanism for transferring anomalies from boundary to the interior of the flow. The instability and eddies are further found to be linked to the along-shore flow length scale and roughness length scale, a finding consistent with numerical simulations of Signell and Geyer (1991). With a rougher ice edge with smaller length scale, a stronger eddy-driven flow is present. In our case, a similar mechanism exists. The formation of cold and fresh anomalies due to basal melting first generates an along-shelf flow. The resulting baroclinic current is perturbed by irregular ice shelf edge, triggering instability that forms eddies, which carry the cold and fresh anomalies offshore to the open ocean. The inclusion of wind forcing, though, can modulate the instabilities through wind-induced oscillations in inflow and outflow, thus further changing the timing and detailed structure of eddies. Chu (1987) studied the fast ice-ocean interaction, and found that even without any prescribed external forcing, the most unstable vertical wave mode can be excited by ice shelf curvatures, which is also consistent with our conclusion here.

A cross-section of one of the eddies simulated in run IIS+WIND+BM (Fig. 8) reveals a lens of cold and fresh water is present in the upper 35 m (Fig. 9). Although the hydrographic structure of the simulated eddy is qualitatively similar to observations, the thickness of the lens is much less than indicated by the VPR survey (Fig. 4). Mechanisms for thickening the lens of cold and fresh water are the subject of the next section.

5. 2-D model simulations

We showed that the cold eddy formation is facilitated by ice shelf roughness and basal melting. Since the thick lenses are observed both within the mesoscale RIS eddies as well as at the RIS edge where the eddies originate, it would therefore be of interest to understand what controls the surface lens thickening at the edge of the ice shelf.

For this purpose, a series of 2-D model sensitivity experiments are carried out with simulations running for 30 days (Table 2). In the first experiment (run WIND), the model is forced by wind only. A strong downwelling-favorable wind event during January 22-28 (Fig. 7) drives the model to form a thick layer of relatively warm and salty surface water (Fig. 10 a, f, k). In the second case (run BM), the wind forcing is turned off and basal melting is turned on. Basal melting leads to a cold and fresh layer adjacent to the ice shelf with buoyancy sufficient to depress the pycnocline by a few tens of meters (Fig. 10 b, g, l). Note that the lack of turbulent kinetic energy input from the wind allows the surface heat flux to establish strong stratification in the surface waters away from the ice shelf. In the third case (run WIND+BM), the combination of wind forcing and basal melt creates a thick (~65 m) lens of cold and fresh water adjacent to the ice shelf (Fig. 10 c, h, m). With wind forcing restored, stratification of the waters north of the ice shelf is similar to that of the first experiment (Cf. Fig. 10 a, f, k and c, h, m).

Although run WIND+BM generates a layer of cold and fresh water reminiscent of that observed near the ice shelf (Fig. 5), it is not as thick. Two more sensitivity experiments are conducted to assess whether or not this discrepancy between the simulated and observed distributions could be explained by differences in the forcing and initial conditions. First, the wind stress was increased by 50% (run HWIND+BM, Fig. 10 d, i, n). This causes a modest deepening of the cold fresh layer, from ~65 m in run WIND+BM to ~75 meters in run HWIND+BM run. Second, as the initial condition is rather *ad hoc* due to limited observations available near ice shelf edge, the temperature, salinity, and density fields in the initial condition were made constant below 50 m, with wind restored as observed (run WIND+BM+WS, Fig.10 e, j, o). This reduction in the stratification allows the cold and fresh layer to deepen to 150 m (below the vertical interval shown in Fig. 10). By reducing the buoyancy Richardson number, the same input of turbulent kinetic energy can homogenize a thicker layer of the upper water column (Abarbanel et al., 1984), thus providing more deepening of the mixed layer by the same amount of surface stress (Trowbridge, 1992).

6. Discussion

The 3-D numerical experiments highlight the role of irregularities in the geometry of the ice shelf edge in stimulating eddy formation. Our results are consistent with the previous findings by Chu (1987), which showed in a semi-analytical framework that unstable wave modes can be excited by along-ice shelf curvatures. This mechanism of eddy formation is also similar to that found in tidal regimes. Both numerical models (Signell and Geyer, 1992) and laboratory observations (Pawlak and MacCready, 2002), illustrate how irregularities in geometry such as ridges and/or headlands can facilitate flow separation, causing vortices to be injected into the ocean interior.

The origin of the cold and fresh near-surface layer adjacent to the RIS can be attributed to basal melting, as evidenced by comparison of the 2-D experiments with and without this effect. However, the properties of this lens may be influenced by other processes not simulated by the model. For example, formation of frazil ice can make the ice shelf water even more buoyant (Jenkins and Bombosch, 1995; Smedsrud and Jenkins, 2004). Moreover, along- ice shelf variability in the RIS plume may be driven by a host of factors, including spatial variations in the cavity geometry, atmospheric forcing, and basal melting rate.

Downwelling-favorable winds were shown to be an important agent of thickening the near-surface lens of cold and fresh water at the edge of the ice shelf. In order to ascertain the degree to which such conditions may prevail at the RIS during summertime, we compute the cumulative upwelling index for each January during the period 2010-2014. First, the upwelling index (UI) is computed according to UI=$\frac{\tau_x}{\rho f}$ (i.e., the offshore component of the Ekman transport) following the method of *Schwing et al.* (1996), where τ_x is the alongshore component of wind stress calculated using the Large and Pond (1981) scheme, and *f* is the local Coriolis parameter. Positive (negative) UI represents upwelling (downwelling) favorable wind conditions. The cumulative UI (CUI) is then computed by integrating the resulting UI over time (i.e., $CUI=\int UI\ dt$) between January 1 and January 31 of each year. The slope of CUI is particularly informative, in that the most downwelling favorable wind conditions are represented by the steepest descending trend shown in CUI. In contrast, a rising trend in CUI indicates that upwelling-favorable wind (negative UI) becomes more dominant.

All Januaries in the time period examined exhibited downwelling-favorable wind conditions (Fig. 11). However, there is significant interannual variability—and our observations were collected during a time period when the downwelling-favorable aspect of the wind was relatively modest. We therefore conclude that wind-forced thickening of the cold and fresh layer may be a frequent occurrence in this regime. However, other mechanisms such as variations in the basal melting rate could be as important or perhaps even more so.

7. Summary and Conclusions

In situ observations along with numerical model simulations were used to investigate the dynamics of cold and fresh eddies near the edge of the Ross Ice Shelf that contained high phytoplankton biomass, dominated by *P. antarctica*.

Idealized 3-D model simulations showed how basal melting can produce a cold and fresh plume adjacent to the RIS, which accelerates a baroclinic current. In the presence of irregularities in the edge of the ice shelf, that current becomes unstable and sheds eddies with the cold and fresh water mass properties of the plume. However, in our simulations the cold and fresh lenses were quantitatively shallower than observed by VPR (35 m vs. 80 m). Idealized 2-D model simulations were then used to investigate the processes that can deepen the cold and fresh surface layer adjacent to the RIS. Wind-induced downwelling can deepen the layer, and the magnitude of this effect depends on the strength of the wind and the underlying stratification—neither of which are particularly well constrained by available data. Sensitivity experiments using the 2-D model document that plausible perturbations to the wind stress and stratification can result in formation of a cold and fresh layer with a vertical extent similar to that observed near the edge of the RIS and in the RIS eddies. A follow-up 3-D simulation with reduced stratification produces thicker lenses within the simulated eddies (not shown). However, we note that the observations document substantial along- ice shelf variability in the density structure. Thus, the thickness of the cold and fresh layer entrained into RIS eddies will vary depending on ambient conditions present at the time of eddy formation. Although our idealized 3-D simulations did not produce eddies with lenses as thick as those observed, we expect that a model with more realistic along- ice shelf variability in water masses, stratification, and surface forcing would do just that.

Acknowledgements

The data used in this paper are archived at the Biological and Chemical Oceanography Data Management Office: http://www.bco-dmo.org/project/2155. Support of this research by the National Science Foundation's United States Antarctic Program is gratefully acknowledged. We thank the officers, crew, and technical personnel on board the R/V *Nathaniel B. Palmer* for their outstanding support during our seagoing operations. O. Kosnyrev and V. Kosnyrev provided assistance with data analysis and figure preparation. YL thanks Drs. John Trowbridge, Jim Ledwell, and Weifeng Gordon Zhang for useful discussions on ocean mixing. YL also thanks Drs. Kenneth Brink and Steve Lentz for insights into instability processes that improved interpretation of the model results. We would also like to acknowledge high-performance computing [Yellowstone (ark:/85065/d7wd3xhc)] provided by NCAR's Computational and Information Systems Laboratory, sponsored by the National Science Foundation. MODIS level 2 satellite data and diffusion attenuation coefficient for downwelling irradiance at 490 nm were made publicly available by NASA Goddard Space Flight Center (http://modis.gsfc.nasa.gov/data/). Complete wind speed data in 2010-2014 at station VITO were kindly provided by Carol Costanza (carol.costanza@ssec.wisc.edu) at University of Wisconsin with addition input from Dr. Douglas MacAyeal (drm7@uchicago.edu) at Univesity of Chicago. Bedmap2 data is archived by British Antarctic Survey (http://nora.nerc.ac.uk/501469/). YL is supported by the Postdoctoral Scholarship Program at Woods Hole Oceanographic Institution, with funding provided by the Dr. George D. Grice Postdoctoral Scholarship.

References

Abarbanel, H. D., Holm, D. D., Marsden, J. E., and Ratiu, T., 1984. Richardson number criterion for the nonlinear stability of three-dimensional stratified flow. Phys. Rev. Lett., 52, 2352.

Arrigo, K. R., Worthen, D., Schnell, A., and Lizotte, M. P., 1998, Primary production in Southern Ocean waters. J. Geophys. Res., 103, 15587-15600.

Arrigo, K. R., van Dijken, G. L., and Strong, A. L. 2015, Environmental controls of marine productivity hot spots around Antarctica. J. Geophys. Res. Oceans, 10.1002/2015JC010888.

Årthun, M., Holland, P. R., Nicholls, K. W., & Feltham, D. L., 2013. Eddy-Driven Exchange between the Open Ocean and a Sub–Ice Shelf Cavity. J. Phys. Oceanogr., 43-11, 2372-2387.

Arzeno, I. B., R.C. Beardsley, R. Limeburner, B. Owens, L. Padman, S. R. Springer, C. L. Stewart, and M. JM., Williams, 2014. Ocean variability contributing to basal melt rate near the ice front of Ross Ice Shelf, Antarctica. J. Geophys. Res. Oceans, 119, 7: 4214-4233.

Carder, K. L., Chen, F. R., Cannizzaro, J. P., Campbell, J. W., and Mitchell, B. G., 2004, Performance of the MODIS semi-analytical ocean color algorithm for chlorophyll-a. Adv. Space Res., 33, 1152-1159.

Clark, D. K., 1997. Algorithm theoretical basis document–Bio-optical algorithms, Case I waters, MODIS algorithm theoretical basis document 18, Version 1.2, available from: http.modis.gsfc.nasa.gov/data/atbd/atbd mod18.

Clarke, A. J., 1978. On wind-driven quasi-geostrophic water movements near fast-ice edges. Deep-Sea Res., 25, 41-51.

Chu, P., 1987. An air-sea feedback mechanism for quasi-geostrophic water movement near a fast shelf-ice edge with a small curvature, Chinese J. Atmos. Sci. 11, 31-42.

Comiso, J.C., McClain, C.R., Sullivan, C.W., Ryan, J.P., Leonard, C.L., 1993. Coastal Zone Color Scanner pigment concentrations in the Southern Ocean and relationships to geophysical surface features. J. Geophys. Res., 98, 2419-2451.

Cushman-Roisin, B., Tang, B., & Chassignet, E. P., 1990. Westward motion of mesoscale eddies. J. Phys. Oceanogr., 20, 758-768.

Davis, C. S., Gallager, S. M., Berman, M. S., Haury, L. R., and Strickler, J. R. ,1992. The video plankton recorder (VPR): design and initial results. Arch. Hydrobiol. Beih, 36, 67-81.

Depoorter, M. A., Bamber, J. L., Griggs, J. A., Lenaerts, J. T. M., Ligtenberg, S. R. M., van den Broeke, M. R., and Moholdt, G. ,2013. Calving fluxes and basal melt rates of Antarctic ice shelves. Nature, 502, 89-92.

Dinniman, M.S., J.M. Klinck and W.O. Smith, Jr., 2003. Cross-shelf exchange in a model of the Ross Sea circulation and biogeochemistry, Deep-Sea Res. II, 50, 3103-3120.

Dinniman, M.S. and J.M. Klinck, 2004. A model study of circulation and cross-shelf exchange on the west Antarctic Peninsula continental shelf, Deep-Sea Res. II, 51, 2003-2022.

Dinniman, M. S., J. M. Klinck, and W. O. Smith Jr., 2007. The influence of sea ice cover and icebergs on circulation and water mass formation in a numerical circulation model of the Ross Sea, Antarctica. J. Geophys. Res., 112, C11013, doi:10.1029/2006JC004036.

Dinniman, M.S., J.M. Klinck and W.O. Smith, Jr, 2011. A model study of Circumpolar Deep Water on the West Antarctic Peninsula and Ross Sea continental shelves.

Deep-Sea Res. II, 58, 1508-1523, doi: 10.1016/j.dsr2.2010.11.013

Dinniman, M.S., J.M. Klinck and E.E. Hofmann, 2012. Sensitivity of Circumpolar Deep Water transport and ice shelf basal melt along the west Antarctic Peninsula to changes in the winds. J. Clim., 25, 4799-4816.

Dumont, D., Gratton, and T. Arbetter, 2010. Modeling Wind-Driven Circulation and Landfast Ice-Edge Processes during Polynya Events in Northern Baffin Bay. J. Phys. Oceanogr., 40, 1356–1372. doi:10.1175/2010JPO4292.1

Falkowski, P. G., and Kolber, Z. ,1995. Variations in chlorophyll fluorescence yields in phytoplankton in the world oceans. Funct. Plant Biol., 22, 341-355.

Foldvik, A., & Kvinge, T. ,1974. Conditional instability of sea water at the freezing point. Deep-Sea Res., 21, 3, 169-174.

Foster, T. D. ,1983. The temperature and salinity fine structure of the ocean under the Ross Ice Shelf. J. Geophys. Res., 88, 2556-2564.

Galton-Fenzi, B.K., 2009. Modelling Ice-Shelf/Ocean Interaction. Ph.D. thesis, University of Tasmania, 151 pp.

Gerringa, L. J. et al., 2012. Iron from melting glaciers fuels the phytoplankton blooms in Amundsen Sea (Southern Ocean): Iron biogeochemistry. Deep-Sea Res. II, 71, 16-31.

Gilmour, A. E., 1979. Ross ice shelf sea temperatures. Science, 203(4379), 438-439.

Gordon, A.L., A.H. Orsi, R. Muench, B.A. Huber, E. Zambianchi, and M. Visbeck, 2009. Western Ross Sea continental slope gravity currents. Deep-Sea Res. II, 56, 796-817.

Goring, D.G., and Pyne, A., 2003. Observations of sea level variability in Ross Sea, Antarctica. NZ J. Mar. Freshwater Res., 37: 241–249.

Gwyther, D. E., Galton-Fenzi, B. K., Dinniman, M. S., Roberts, J. L., & Hunter, J. R. , 2015. The effect of basal friction on melting and freezing in ice shelf–ocean models. Ocean Modell., 95, 38-52.

Haidvogel, D. B., Arango, H., Budgell, W. P., Cornuelle, B. D., Curchitser, E., Di Lorenzo, E., ... and Wilkin, J. ,2008. Ocean forecasting in terrain-following coordinates: Formulation and skill assessment of the Regional Ocean Modeling System. J. Comput. Phys., 227, 3595-3624.

Häkkinen, S., 1986: Coupled ice-ocean dynamics in the marginal ice zones, upwelling/downwelling and eddy generation. J. Geophysical Research, 91, 819–832.

Holland, D. M., and Jenkins, A., 1999. Modeling thermodynamic ice-ocean interactions at the base of an ice shelf. J. Phys. Oceanogr., 29, 1787-1800.

Horgan, H.J., R.T. Walker, S. Anandakrishnan, and R.B. Alley, 2011. Surface elevation changes at the front of the Ross Ice Shelf: Implications for basal melting. J. Geophys. Res., 116, C02005.

Jacobs, S. S., Amos, A. F., & Bruchhausen, P. M., 1970. Ross Sea oceanography and Antarctic bottom water formation. Deep-Sea Res., 17, 6, 935-962.

Jacobs, S. S., Gordon, A. L., and Ardai, J. L., 1979. Circulation and melting beneath the Ross Ice Shelf, Science, 203, 439-443.

Jacobs, S.S., Fairbanks, R.G., and Horibe, Y., 1985. Origin and evolution of water masses near the Antarctic continental margin: evidence from $H_2{}^{18}O$/ $H_2{}^{16}O$ ratios in seawater. in: Oceanology of the Antarctic Continental Shelf (S. Jacobs, ed.), Antarct. Res, Ser., American Geophysical Union, Washington D.C., 43, 59-85.

Jacobs, S. S. (1992). Is the Antarctic ice sheet growing? Nature, 360, 29-33.

Jacobs, S. S., Hellmer, H. H., & Jenkins, A. ,1996. Antarctic ice sheet melting in the Southeast Pacific. Geophys. Res. Lett., 23, 957-960.

Jacobs, S. S., Jenkins, A., Giulivi, C. F., and Dutrieux, P. ,2011. Stronger ocean circulation and increased melting under Pine Island Glacier ice shelf. Nature Geosci., 4, 519-523.

Jenkins, A., and Doake, C. S. M., 1991. Ice-ocean interaction on Ronne Ice Shelf, Antarctica. J. Geophys. Res. Oceans, 96, 791-813.

Jenkins, A., and Bombosch, A., 1995. Modeling the effects of frazil ice crystals on the dynamics and thermodynamics of ice shelf water plumes. J. Geophys. Res. Oceans, 100, 6967-6981.

Keys, H. J., Jacobs, S. S., and Barnett, D., 1990. The calving and drift of iceberg B-9 in the Ross Sea, Antarctica. Antarctic Sci., 2, 243-257.

Klinck, J. M., Hofmann, E. E., Beardsley, R. C., Salihoglu, B., and Howard, S., 2004. Water-mass properties and circulation on the west Antarctic Peninsula Continental Shelf in austral fall and winter 2001. Deep-Sea Res. II, 51, 1925-1946.

Klinck, J. M., and M. S. Dinniman, 2010. Exchange across the shelf break at high southern latitudes. Ocean Sci., 6, 513–524.

Krauss, E.B., Turner, J.S., 1967. A one-dimensional model of the seasonal thermocline. Tellus 19, 98–105.

Large, W. G., and Pond, S., 1981. Open ocean momentum flux measurements in moderate to strong winds. J. Phys. Oceanogr., 11, 324-336.

Large, W. G., McWilliams, J. C., and Doney, S. C., 1994. Oceanic vertical mixing: A review and a model with a nonlocal boundary layer parameterization. Rev. Geophys., 32, 363-404.

Losch. M., 2008. Modeling ice shelf cavities in a z coordinate ocean general circulation model. J. Geophys. Res. Oceans, 113, C08043.

MacAyeal, D. R., 1984. Thermohaline circulation below the Ross Ice Shelf: A consequence of tidally induced vertical mixing and basal melting. J. Geophys. Res. Oceans, 89, 597-606.

MacAyeal, D. R., 1985. Tidal rectification below the Ross Ice Shelf, Antarctica. Antarct. Res. Ser., 43, 109-132.

Makinson, K., Schröder, M., & Østerhus, S., 2006. Effect of critical latitude and seasonal stratification on tidal current profiles along Ronne Ice Front, Antarctica. J. Geophys. Res., Oceans, 111, C03022.

Marchesiello, P., J.C. McWilliams, and A.F. Shchepetkin, 2001. Open boundary conditions for long-term integration of regional oceanic models. Ocean Modell., 3,

1-20.
McGillicuddy, D.J., Sedwick, P.N., Dinniman, M.S., Arrigo, K.R., Bibby, T.S., Greenan, B.J.W., Hofmann, E.E., Klinck, J.M., Smith, W.O., Mack, S.L., Marsay, C.M., Sohst, B.M., and G.L. van Dijken ,2015. Iron supply and demand in an Antarctic shelf ecosystem, Geophys. Res. Lett., 42, 8088–8097.
Mellor, G. L., and Blumberg, A. F., 1985. Modeling vertical and horizontal diffusivities with the sigma coordinate system. Mon. Weather Rev., 113, 1379-1383.
Nicholls, K. W., Padman, L., Schröder, M., Woodgate, R. A., Jenkins, A., & Østerhus, S., 2003. Water mass modification over the continental shelf north of Ronne Ice Shelf, Antarctica. J. Geophys. Res. Oceans, 108, 3260.
Niiler, P.P., Kraus, E.B., 1977. One-dimensional models of the Upper Ocean. In: Krauss, E.B. (Ed.), Modeling and Prediction of the Upper Layers of the Ocean. Pergamon, New York, pp. 143–172.
Niebauer, H. J. ,1982. Wind and melt driven circulation in a marginal sea ice edge frontal system: a numerical model. Cont. Shelf Res., 1, 49-98.
Orsi, A.H., Smethie Jr., W.M., and Bullister, J.L., 2002. On the total input of Antarctic Waters to the Deep Ocean: a preliminary estimate from chlorofluorocarbon measurements. J. Geophys. Res. Oceans, 107, 3122.
Orsi, A.H. and Wiederwohl, C.L., 2009. A recount of Ross Sea waters. Deep Sea Research II, 56, 13-14, doi:10.1016/j.dsr2.2008.10.033.Pawlak, G., and MacCready, P., 2002. Oscillatory flow across an irregular boundary. J. Geophys. Res. Oceans, 107, 4-1.
Pritchard, H. D., Ligtenberg, S. R. M., Fricker, H. A., Vaughan, D. G., Van den Broeke, M. R., and Padman, L. ,2012. Antarctic ice-sheet loss driven by basal melting of ice shelves. Nature, 484, 502-505.
Rignot, E., Jacobs, S., Mouginot, J., and Scheuchl, B., 2013. Ice-shelf melting around Antarct. Science, 341, 266-270.
Schwing, F. B., O'Farrell, M., Steger, J. M., and Baltz, K., 1996. Coastal Upwelling indices west coast of North America. NOAA Tech. Rep., NMFS SWFSC, 231, 144p.
Shchepetkin, A.F., McWilliams, J.C., 1998. Quasi-monotone advection schemes based on explicit locally adaptive dissipation. Mon. Weather Rev., 126, 1541–1580.
Shchepetkin, A. F., & McWilliams, J. C., 2003. A method for computing horizontal pressure-gradient force in an oceanic model with a nonaligned vertical coordinate. J. Geophys. Res. Oceans, 108, 1-33.
Shchepetkin, A. F., and McWilliams, J. C., 2005. The regional oceanic modeling system (ROMS): a split-explicit, free-surface, topography-following-coordinate oceanic model. Ocean Modell. 9, 347-404.
Shepherd, A. et al., 2010. Recent loss of floating ice and the consequent sea level contribution. Geophys. Res. Lett., 37, L13503.
Shepherd, A. et al., 2012. A reconciled estimate of ice-sheet mass balance. Science, 338, 1183-1189.

Signell, R., P., and W. R., Geyer, 1991. Transient eddy formation around headlands. J. Geophys. Res. Oceans, 96: 2561-2575.

Smedsrud, L. H., and Jenkins, A., 2004. Frazil ice formation in an ice shelf water plume. J. Geophys. Res. Oceans, 109, C03025.

Smethie Jr., W.M. and Jacobs, S.S., 2005. Circulation and melting under the Ross Ice Shelf: estimates form evolving CFC, salinity and temperature fields in the Ross Sea. Deep-Sea Res. I, 52, 959-978.

Smith Jr, W. O., and D. J. McGillicuddy et al., Ghost colonies of Phaeocystis: distribution and abundance in the Ross Sea, in preparation.

Stern, A. A., Dinniman, M. S., Zagorodnov, V., Tyler, S. W., and Holland, D. M. 2013. Intrusion of warm surface water beneath the McMurdo Ice Shelf, Antarctica. J. Geophys. Res. Oceans, 118, 7036-7048.

Trowbridge, J. H. ,1992. A simple description of the deepening and structure of a stably stratified flow driven by a surface stress. J. Geophys. Res. Oceans, 97, 15529-15543.

Whitworth, T., and Orsi, A. H., 2006. Antarctic Bottom Water production and export by tides in the Ross Sea. Geophys. Res. Lett., 33, L12609.

Appendix A. Model sensitivity to horizontal diffusivity

In numerical models, the background mixing coefficients are chosen based on grid length scale and a time scale for energy dissipation. These parameters should be chosen to preserve the dynamics of interest (Mellor and Blumberg, 1985), damping out fluctuations that are not resolved by the grid (e.g. 2 Δx waves). In the harmonic case, the background horizontal diffusivity is defined as $(\Delta x/\pi)^2/\Delta t$, where Δt is damping time scale. Our grid resolution is Δx=500 m, so a practical range for Δt is 3~12 hours, therefore resulting in a horizontal diffusivity coefficient of roughly 0.5~2 m^2s^{-1}. We performed a series of experiments to test the sensitivity of lens thickness near the ice shelf edge to this parameter. Results show that by changing viscosity from 0.5 to 4 $m^2\,s^{-1}$, the lens thickness is only shallowed by ~2-3 meters, which is an order of magnitude or more less than the amplitude of the simulated signal. In the simulations presented herein, the diffusion coefficient is 0.5 m^2s^{-1}, a value that is smaller than that usually used with the naturally dissipative upstream advection scheme (Shchepetkin and McWilliams, 1998; Dinniman et al., 2003).

Appendix B. Details for the basal melting and mechanical forcing by the ice shelf edge

Here we briefly summarize the representation of the ice shelf in the model. The ocean water underneath has interactions with the ice shelf through thermodynamics. Under the ice shelf, the upper boundary for the surface model layer is not at sea level because it conforms to the ice shelf base. The hydrostatic pressure gradient force calculation thus accounts for the possibilities that the top layer of the ocean may have a significant slope due to the ice shelf (Shchepetkin and McWilliams, 2003), assuming that the ice is in isostatic equilibrium. While there are concerns about pressure gradient (PG) errors at the ice shelf front in terrain following coordinate models (e.g. Losch, 2008), the PG algorithm used in ROMS (Shchepetkin and McWilliams, 2003) has been explicitly shown to limit these issues in the case of ice shelf fronts (Galton-Fenzi, 2009). A 2-D run without surface forcing or basal melting shows that the PG errors cause only small perturbations to the density field. After several hours of simulation, the solution stabilizes. Changes to the initial density field (~10^{-4} kg m^3) and the associated velocities (~10^{-6} m s^{-1}) are essentially small. This suggests that the PG error is not a problem in our simulations.

Atmospheric forcing of waters underneath the ice shelf is set to zero, assuming that fluid is isolated from the atmosphere. Friction between the ice shelf and the water is computed as a quadratic stress with a coefficient of 3.0×10^{-3}.

At the water-ice shelf interface, a viscous sublayer model is used with three equations representing the conservation of heat, the conservation of salt, and a linearized version of the formula for the freezing point of sea water as a function of salinity and pressure. Free variables in these equations are T_b, S_b, and $\frac{\partial h}{\partial t}$, which stand for temperature, salinity at the ice shelf base, and melting rate, respectively. $\frac{\partial h}{\partial t}$ is <0 for melting and >0 for freezing.

The conservation of heat across the ocean-ice shelf boundary is:

$$\rho_i (L - C_{pi}\Delta T)\frac{\partial h}{\partial t} = \rho C_{pw}\gamma_T (T_b - T_w) \qquad \text{(B.1)}$$

where ρ_i is ice density (930 kg m^{-3}), L is the latent heat of fusion (3.34×10^5 J kg^{-1}), C_{pi} is the heat capacity of ice (2000 J (kg ℃)$^{-1}$), and ΔT is the temperature difference between the ice shelf interior and the freezing temperature at the ice shelf base. However, in our simulations we did not consider the impact of heat conduction through the ice shelf, therefore $\Delta T=0$ and the ice shelf is assumed to be perfectly insulating. ρ is the density of water, C_{pw} is the heat capacity of sea water at 0 ℃ (4000 J (kg ℃)$^{-1}$), γ_T is the turbulent exchange coefficient for heat and is computed as a function of the friction velocity (Holland and Jenkins, 1999), and T_w is the water temperature in the uppermost grid box.

The conservation of salt across the ocean-ice shelf boundary is written as:

$$\rho_i S_b \frac{\partial h}{\partial t} = \rho\gamma_s (S_b - S_w) \qquad \text{(B.2)}$$

where γ_s is the turbulent exchange coefficient for salt, and is computed as a function of the friction velocity (Holland and Jenkins, 1999), and S_w is the salinity in the uppermost grid box. The linearized equation for the freezing point of sea water (Foldvik and Kvinge, 1974) defines T_b as

$$T_b = 0.0939 - 0.057 S_b + 7.6410 \times 10^{-4} h \qquad \text{(B.3)}$$

where h is the depth below the sea level.

For simplicity, the draft and extent of the ice shelf do not change over time in the model, a reasonable approximation for simulations of this duration also made in previous simulations (Dinniman et al., 2007; Stern et al., 2013).

3-D experiments	Ice shelf edge	Basal melting	Surface wind forcing
SIS+WIND+BM	Straight	ON	ON
IIS+WIND+BM	Irregular	ON	ON
IIS+BM	Irregular	ON	OFF

Table 1. List of 3-D experiments performed in this study. In the left column, SIS and IIS stand for “straight ice shelf” and “irregular ice shelf” respectively; BM stands for basal melting.

2-D experiments	Basal melting	Surface wind forcing	Initial condition
WIND	OFF	Observed	CTD 58
BM	ON	OFF	CTD 58
WIND+BM	ON	Observed	CTD 58
HWIND+BM	ON	Observed ×1.5	CTD 58
WIND+BM+WS	ON	Observed	CTD 58, constant density below 50m

Table 2**.** List of 2-D experiments performed in this study. In the left column, HWIND, WS, and BM stand for “high wind stress”, “weak stratification”, and “basal melting”, respectively.

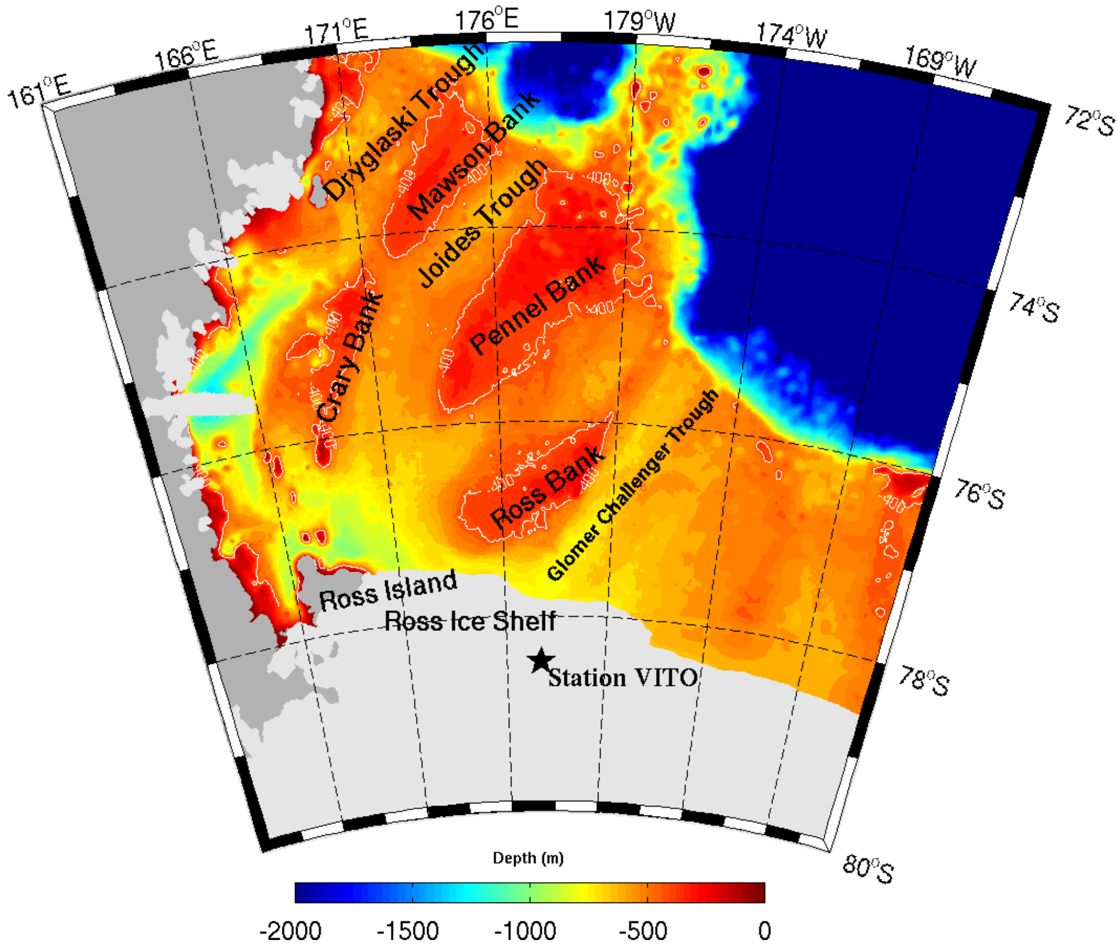

Fig. 1. Bathymetric map of the Ross Sea based on Bedmap2 bottom elevation data made available by the British Antarctic Survey (http://nora.nerc.ac.uk/501469/). White contours are the 400 m isobath. The Pentagram indicates the location for Antarctic meteorological station VITO. The permanent ice shelf is shown in light gray, and land in dark gray.

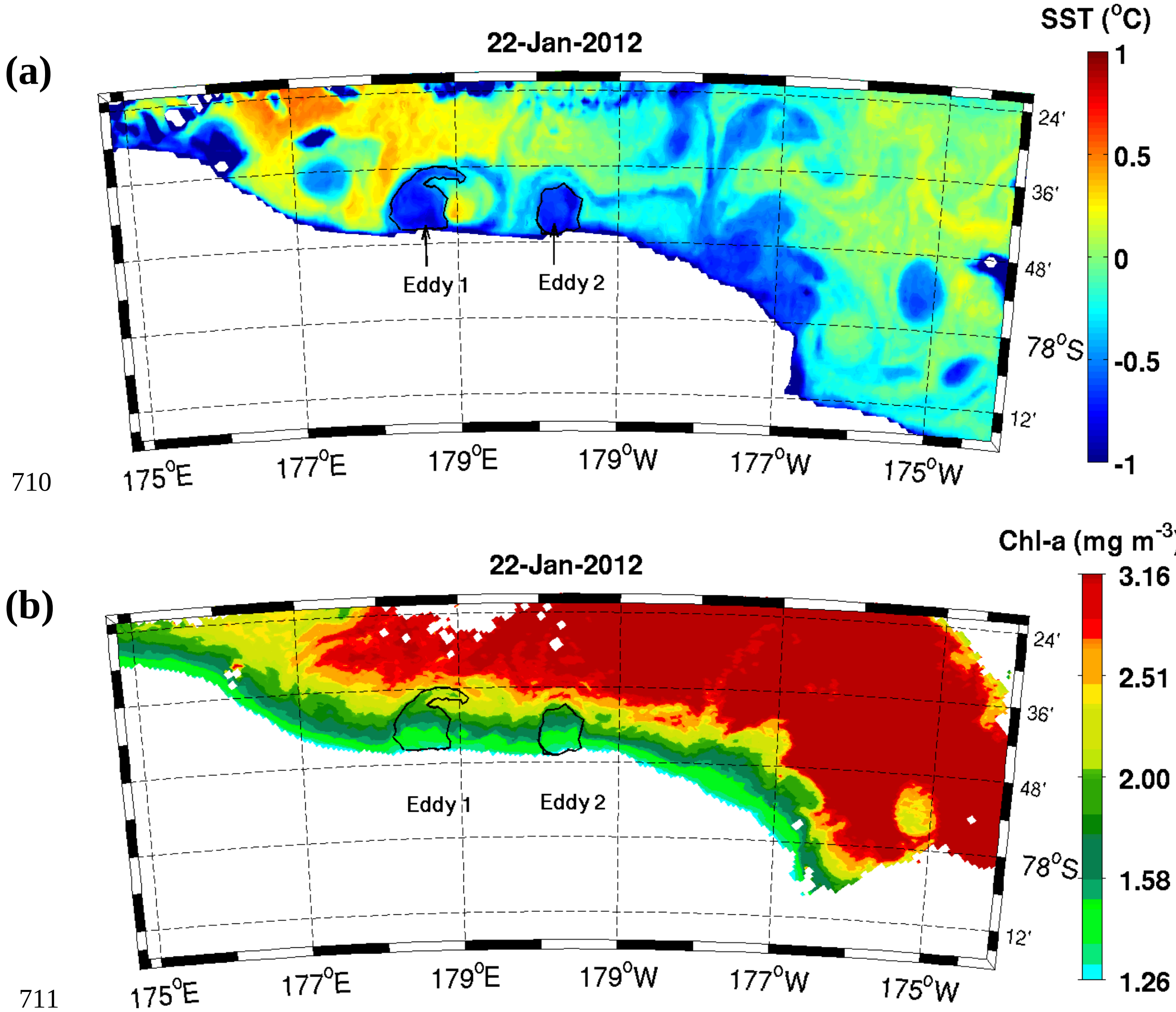

Fig. 2. Moderate Resolution Imaging Spectroradiometer (MODIS) level 2 (1 km resolution) SST and Chl-a images for January 22, 2012. Black lines outline the two ice shelf eddies. Satellite data provided by NASA's Goddard Space Flight Center (http://modis.gsfc.nasa.gov/data/).

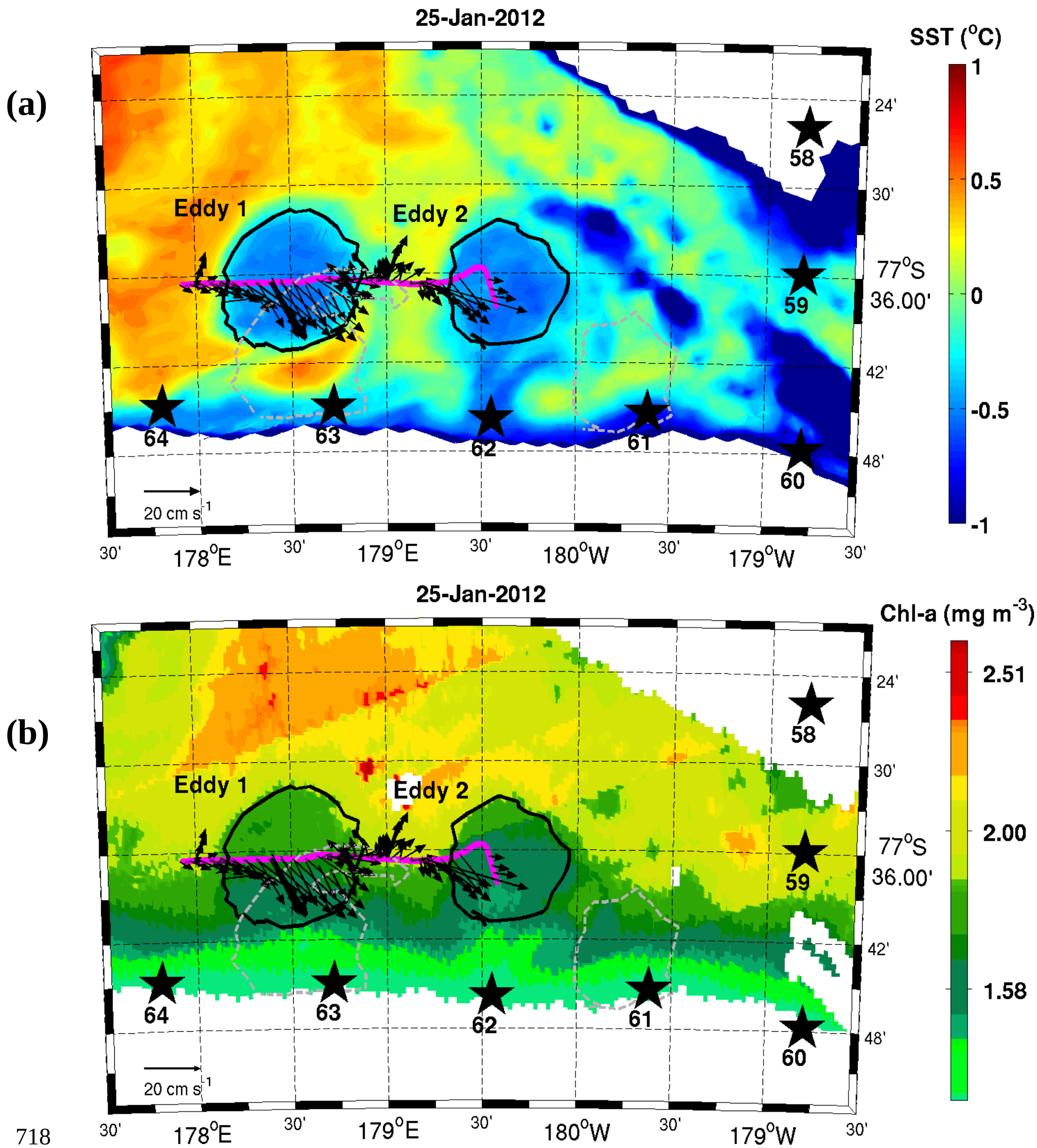

Fig. 3. Zoom in view of MODIS level 2 SST and Chl-a images for January 25, 2012. Note that for visualization purposes, the Chl-a concentrations along swaths are projected into a uniformly spaced longitude-latitude coordinate. The magenta line indicates the cross-eddy transect on January 26, 2012 depicted in Fig. 4. Black solid (gray dashed) lines outline the two ice shelf eddies on January 25 (22), and pentagrams indicate CTD station locations (58-64) during the Ross Ice Shelf survey January 25-26, 2012. Vectors stand for the depth-averaged current over top 200 m during the survey. Velocity scale factor is shown at the lower left.

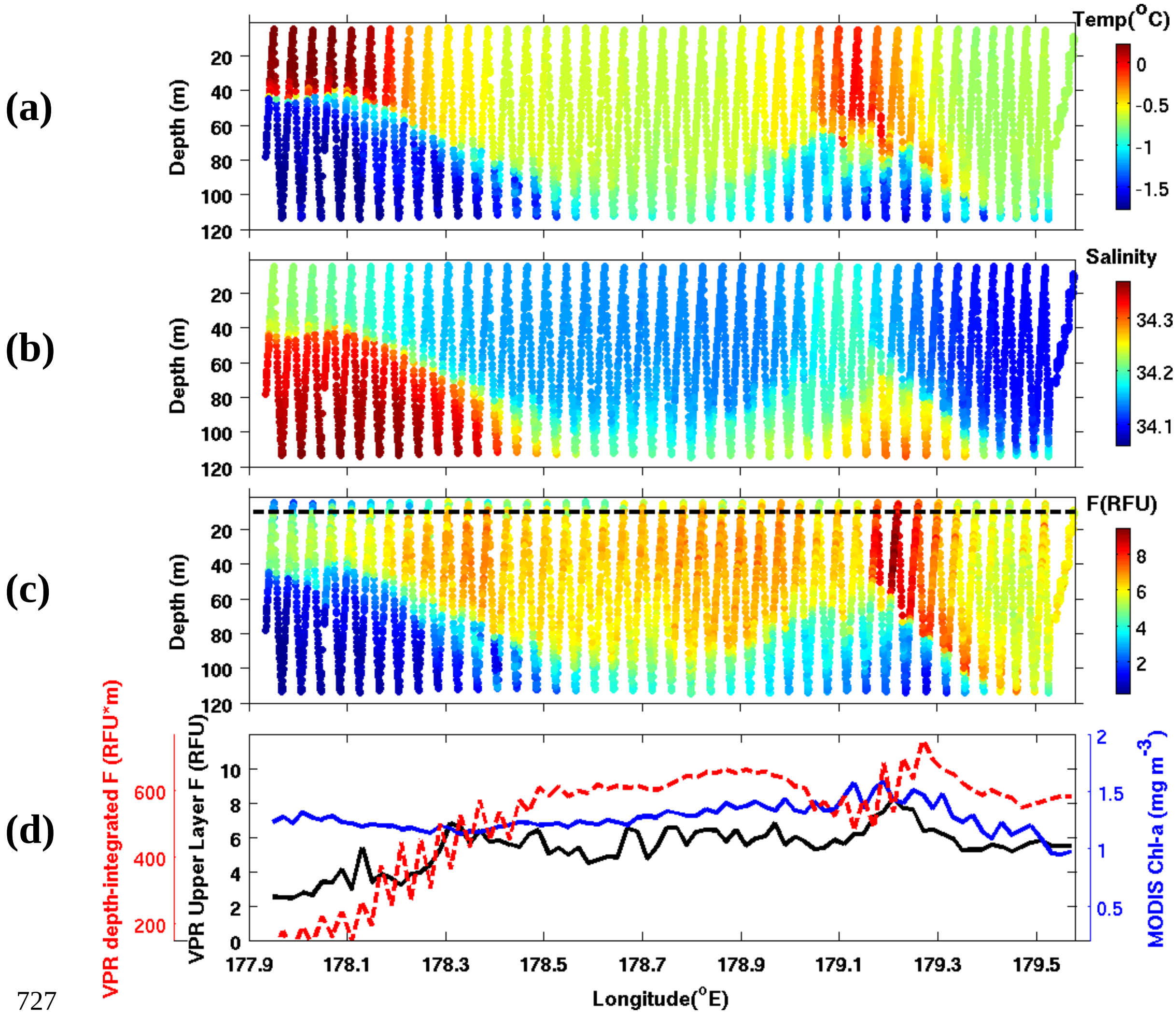

Fig. 4. Profiles of temperature, salinity and fluorescence (F in relative fluorescence units, or RFU) from the VPR survey depicted by the magenta line in Fig. 3. In panel (c), the depth of the second optical depth is plotted in black dashed line. Bottom panel shows the weighted VPR fluorescence within the top 10 m (black), MODIS surface Chl-a concentration extracted along the VPR track (blue), and depth-integrated VPR fluorescence (red) within the top 100m.

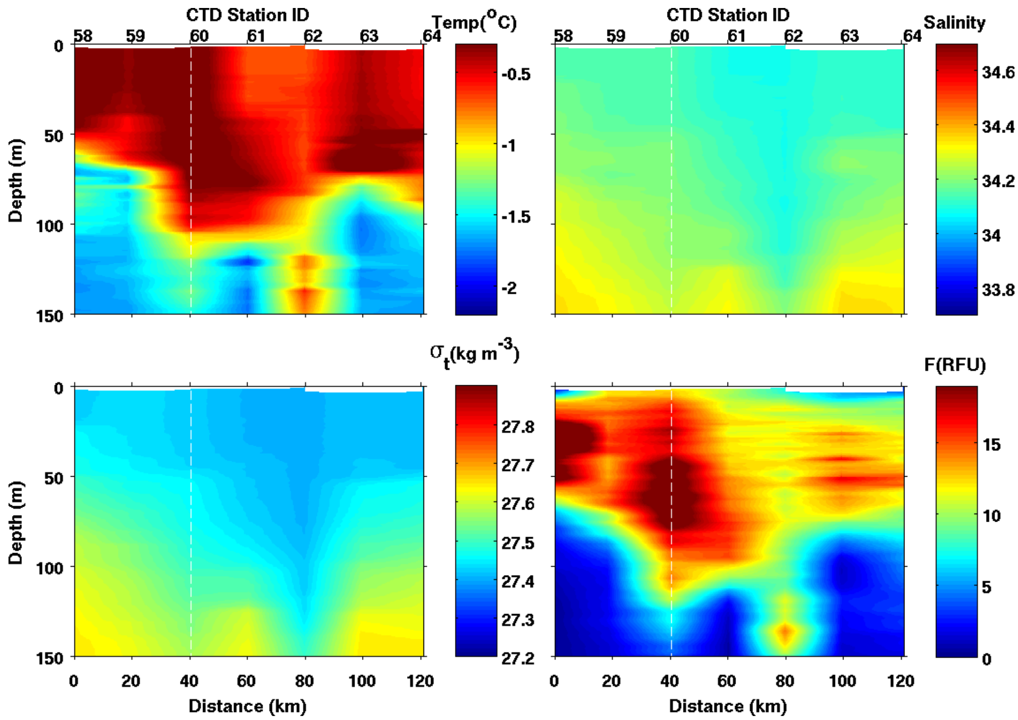

Fig. 5. Temperature, salinity, σ_t and fluorescence (F in fluorescence units, or RFU) observations for RIS CTD casts (see Fig. 3 for station positions). The white dashed line indicates the station where the transect orientations shift from north-south to east-west.

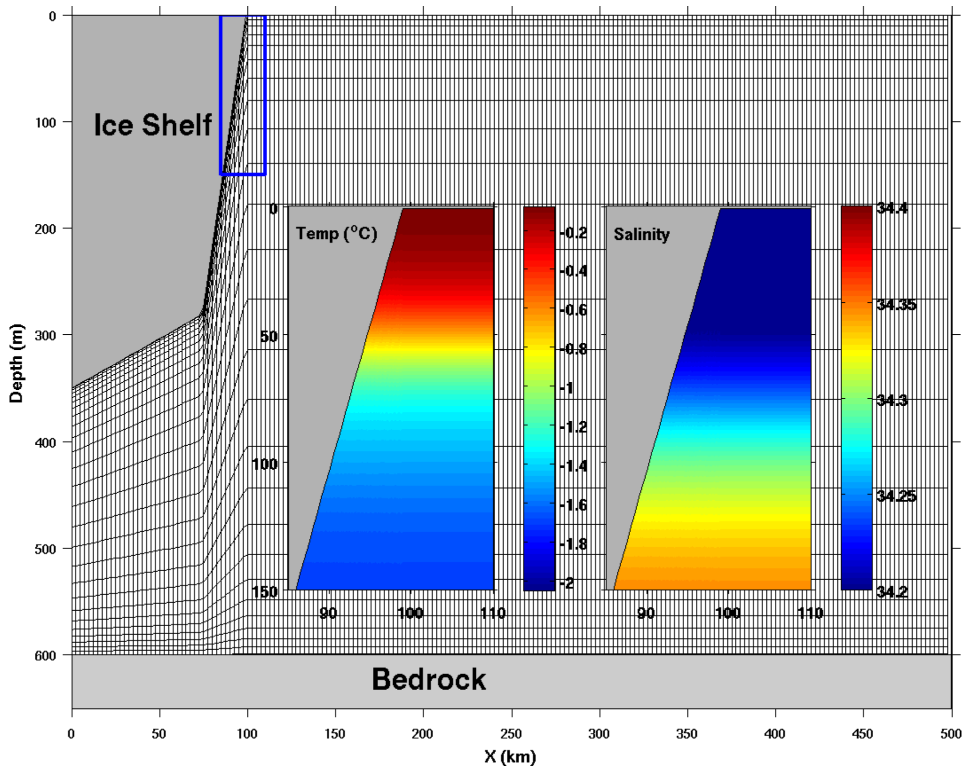

Fig. 6. Cross-shelf view of ice shelf configuration and model grid. The grids are decimated such that each cell represents 5 by 4 grid points. Insets show zoomed-in views of the temperature and salinity profiles in the initial condition on the upper part of the ice shelf (blue rectangle).

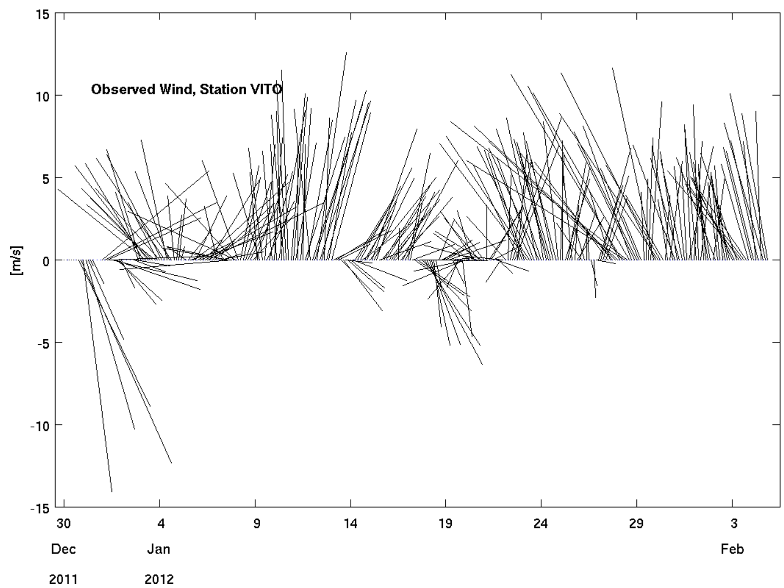

Fig. 7. 10-meter wind record from meteorological station VITO (see Fig. 1 for station location).

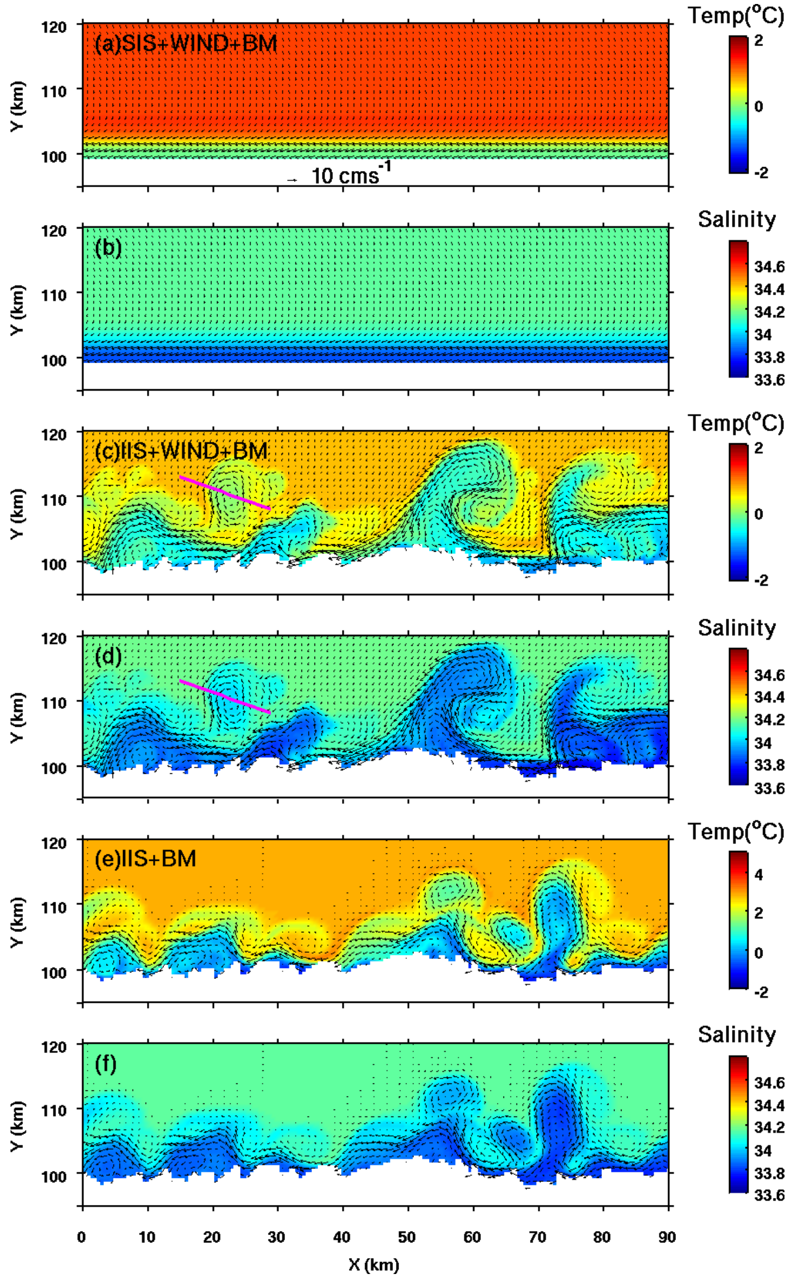

Fig. 8. Snapshots of surface temperature and salinity (surface velocity vectors overlaid) at model day 25 listed in Table 1: (a, b) SIS+BM+WIND; (c, d) IIS+BM+WIND; (e, f) IIS+BM. The magenta line in panels c and d indicates the location of a cross-eddy transect shown in Fig. 9.

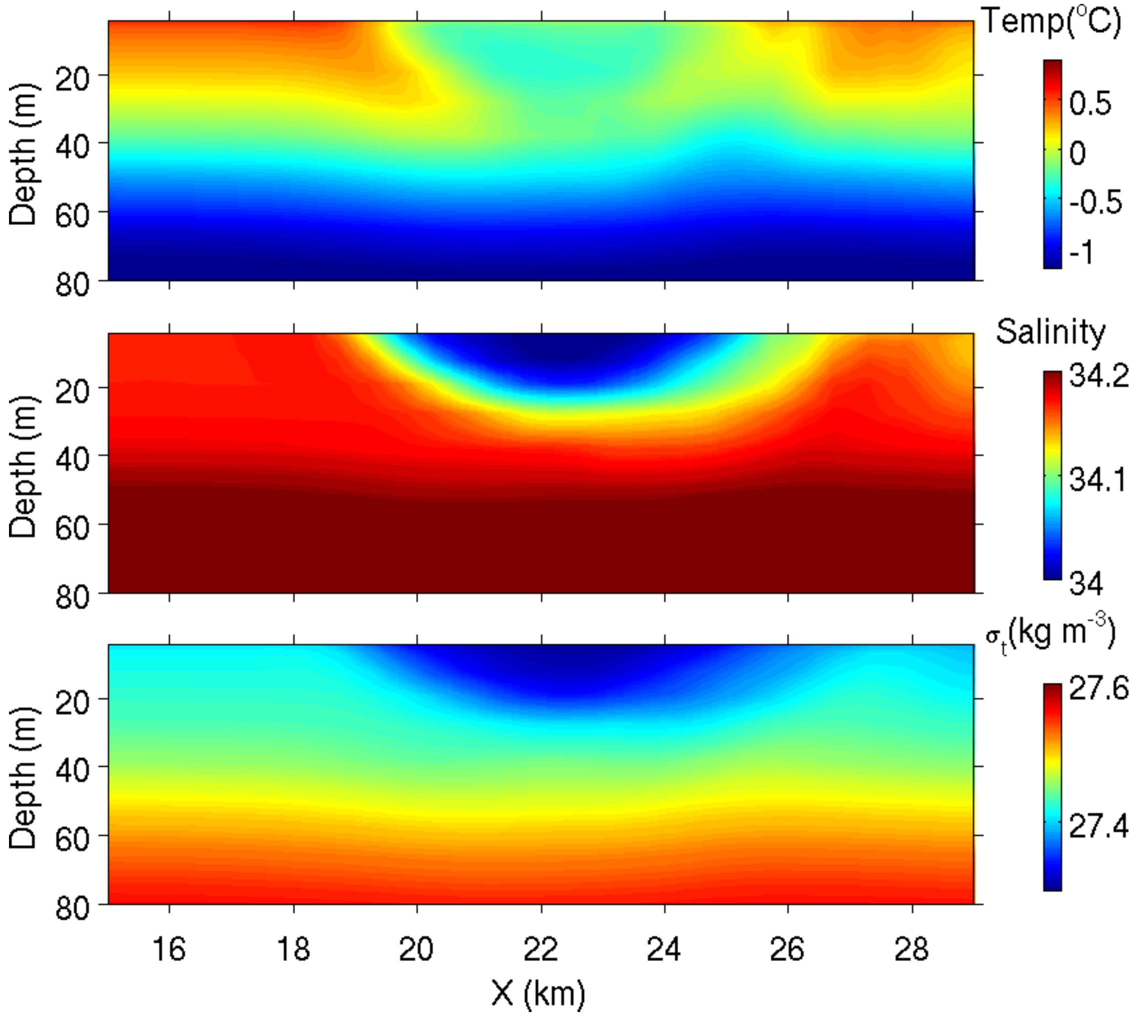

Fig. 9. Vertical transect of temperature, salinity and σ_t for the cross-eddy transect indicated in Fig. 8.

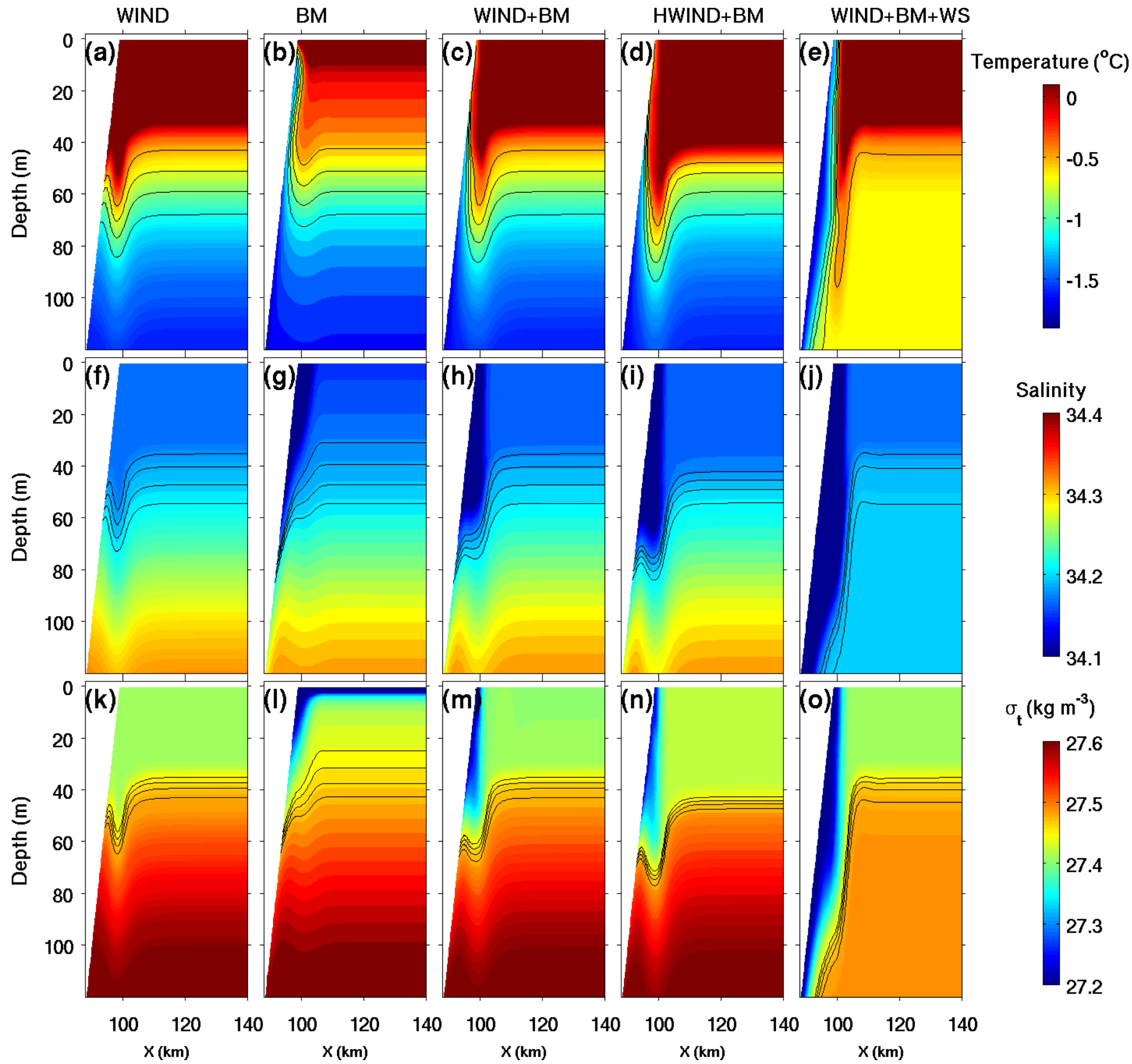

Fig. 10. Snapshots of temperature, salinity and σ_t on model day 29.5 for 2-D experiments listed in Table 2: (a, f, k) WIND; (b, g, l) BM; (c, h, m) WIND+BM; (d, i, n) 2D HWIND+BM; (e, j, o) 2D WIND+BM+WS. Solid contours highlight key isotherms (-1.1 to -0.5 ℃ at intervals of 0.2 ℃), isohalines (34.18 to 34.21 at intervals of 0.01), and isopycnals (27.45 to 27.48 kg m^{-3}at intervals of 0.01 kg m^{-3}).

.

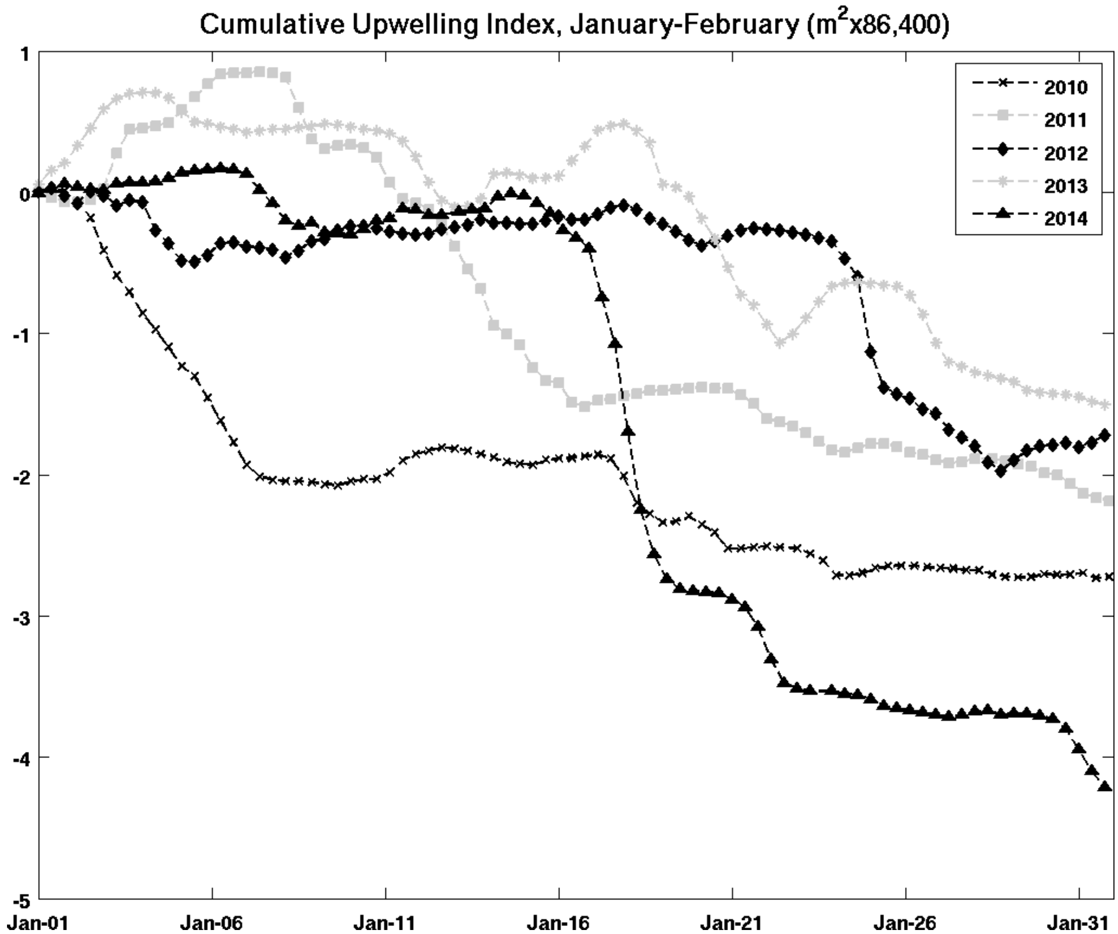

Fig. 11. Cumulative Upwelling Index (CUI) for the Januaries in 2010-2014.